Structural, magnetic, and optical properties of BiFeO$_3$ and Bi$_2$FeMnO$_6$ epitaxial thin films: An experimental and first-principles study

Lei Bi, Alexander R. Taussig, Hyun-Suk Kim, Lei Wang, Gerald F. Dionne,[*] D. Bono, K. Persson, Gerbrand Ceder, and C. A. Ross

Department of Materials Science and Engineering, Massachusetts Institute of Technology, Cambridge, Massachusetts 02139, USA

BiFeO$_3$ and Bi$_2$FeMnO$_6$ films were epitaxially grown on SrTiO$_3$ (001) substrates by pulsed-laser deposition, and their structural, magnetic, magneto-optical and optical properties were measured. In Bi$_2$FeMnO$_6$, Fe is mainly present in the 3+ valence state, while Mn shows multivalence states. Bi$_2$FeMnO$_6$ exhibits low magnetization at room temperature and at 5 K indicating there is no significant *B*-site ordering. The BiFeO$_3$ film shows high optical transparency, while Bi$_2$FeMnO$_6$ shows high absorption loss in the infrared. Density-functional theory modeling of BiFeO$_3$, BiMnO$_3$ and Bi$_2$FeMnO$_6$ was carried out by applying the generalized gradient approximation (GGA) and GGA+U methods. The formation enthalpy of ordered Bi$_2$FeMnO$_6$ is positive for several crystal symmetries and for ferromagnetic (FM) or antiferromagnetic (AFM) spin structures at 0 K temperature, indicating *B*-site ordering is not favored. The electronic structure calculations are consistent with the electronic and optical properties of these films.

PACS number(s): 77.80.−e, 75.50.Ee, 78.20.−e

I. INTRODUCTION

Ordered double perovskites, in which two different *B*-site cations form a superlattice within the ABO$_3$ perovskite structure, have attracted great interest recently.[1–5] Materials with such a structure may possess both ferromagnetic and ferroelectric, or ferromagnetic and ferroelastic properties, and are therefore multiferroics.[6–8] Among these materials, room temperature (RT) ordered double perovskites with bismuth on the *A* site are particularly interesting. Due to the large orbital radius of the Bi $6s^2$ lone pairs, the crystal structure of bismuth-based perovskites is usually distorted to low symmetries, producing large spontaneous ferroelectric polarization along certain crystallographic directions.[9] At the same time, *B*-site ordering of transition-metal ions may make such materials ferromagnetic or ferrimagnetic. If the magnetic and ferroelectric properties couple with each other, these materials are intrinsic magnetoelectric multiferroics. Integrated magneto-optical isolators could provide another application for Bi-based ordered double perovskites.[10,11] A magneto-optical isolator makes use of Faraday rotation to control the polarization direction of incident light. Due to their good lattice match with silicon, perovskite materials, especially orthoferrites (AFeO$_3$), might be suitable candidates for integrated isolators.[12] In order to obtain high Faraday rotation in perovskites, one has to line up most of the orbital angular momentum vectors of the active ionic electric dipoles along a macroscopic direction. This is usually achieved by spin-orbit coupling in a ferromagnetic or ferrimagnetic material. In other words, efficient Faraday rotators are usually ferromagnetic or ferrimagnetic at RT. In ordered double perovskites with Curie temperature (T_C) above RT, the spins and orbital angular momentum vectors of the two types of GGA+U-site ions align along their own macroscopic directions when magnetized, providing a net Faraday rotation at certain wavelengths.[12] Meanwhile, Bi^{3+} ions have strong covalent interactions with the octahedral complexes, which enhance the nondegeneracy of the spin-orbit coupling levels as

well as the Faraday rotation of the material.[13,14]

Among the bismuth perovskites, perhaps BiFeO$_3$ is the most systematically studied.[15–17] The Bi$_2$FeMnO$_6$ bulk crystal belongs to the $R3c$ space group. The unit cell of BiFeO$_3$ can be considered to be a deformed ideal cubic perovskite. By moving Bi and Fe atoms along the pseudocubic [111] direction and O atoms along the pseudocubic ⟨110⟩ directions, the unit cell is elongated with the neighboring octahedrons rotated in different directions about the [111] axis.[18] BiFeO$_3$ is antiferromagnetic with a Néel temperature of $T_N \sim 640$ K.[19,20] The Fe spins form a *G*-type antiferromagnetic (*G*-AFM) structure, in which the spins are coupled ferromagnetically in the pseudocubic (111) planes and antiferromagnetically between neighboring (111) planes, so that each Fe atom couples antiferromagnetically with its nearest Fe neighbors.[21] Besides BiFeO$_3$, another bismuth perovskite, BiMnO$_3$, is also well studied because of its multiferroic properties at low temperature.[22] Due to the Bi $6s^2$ lone pairs, the unit cell of the BiMnO$_3$ bulk crystal is distorted to $C2$ symmetry at and below room temperature.[23] In contrast to BiFeO$_3$, BiMnO$_3$ is ferromagnetic with $T_C \sim 105$ K.[24] This is because ferromagnetic rather than antiferromagnetic superexchange between the e_g orbitals of neighboring Mn^{3+} ions is favored in the distorted unit cell.[25–27] There are also several experimental studies on BiFe$_{1-x}$Mn$_x$O$_3$ bulk crystals and thin films.[28–31] A general finding is that incorporation of Fe in the Mn-rich side drives the material from ferromagnetic to antiferromagnetic, while adding Mn in the Fe-rich side results in higher saturation magnetization at room temperature.

Despite these previous studies, there are several questions remaining. First, is *B*-site ordering likely to occur in certain double perovskite systems (specifically BiFe$_{1-x}$Mn$_x$O$_3$ in this study)? Previous experimental results indeed show that incorporating Mn into the BiFeO$_3$ lattice enhanced the magnetization,[30,31] but whether this is caused by local *B*-site ordering is unclear. Second, for magneto-optical isolator applications, how do the Bi and *B*-site ions influence the optical and magneto-optical properties of these perovskites? Al-

though $YFeO_3$ and rare-earth-based orthoferrites show high optical transparency ($\alpha < 0.5$ cm^{-1}) and high Faraday rotation constant at 1550 nm wavelength,[32,33] as far as we know, the infrared optical and magneto-optical properties of bismuth perovskites and bismuth double perovskites have not been reported. In order to answer these questions, we first examine the spin ordering influences due to local magnetic exchange interactions among the various possible cation combinations. We then employ both experimental and first-principles calculation methods to investigate the structural, magnetic, and optical properties of $BiFeO_3$ and Bi_2FeMnO_6 epitaxial thin films.

II. SPIN ORDERING CONSIDERATIONS

Based on anticipated effects of local interactions in a generic ABO_3 perovskite lattice, the magnetic moment and Faraday rotation should be dominated by antiferromagnetic spin ordering. In a stoichiometric specimen of B or Bi_2FeMnO_6, the most stable valence for either Fe or Mn is 3+. For $Fe^{3+}(3d^5)$, the five spins are aligned in a half-filled $3d$ shell ($t_{2g}^3 e_g^2$) high-spin configuration as dictated by Hund's rule; for the same reason, $Mn^{3+}(3d^4)$ is in a high-spin $t_{2g}^3 e_g^1$ arrangement in octahedral B sites that is further stabilized by a strong Jahn-Teller axial distortion along the z axis.

An important characteristic of the perovskite lattice is the 180-degree cation-anion-cation bonds that involve the e_g orbitals in bonding/antibonding linkages with the oxygen $2p$ orbitals, while relegating the t_{2g} orbitals to nonbonding roles. According to the Goodenough-Kanamori rules for 180-degree superexchange couplings,[25] the expectations for five possible combinations in these compounds are

$$(1) Fe^{3+} - O^{2-} - Fe^{3+} \quad \text{strong AFM,}$$

$$(2) Mn^{3+} - O^{2-} - Mn^{3+} \quad \text{vibronic FM/AFM,}$$

$$(3) Fe^{3+} - O^{2-} - Mn^{3+} \quad \text{vibronic AFM/FM,}$$

$$(4) Fe^{2+} - O^{2-} - Mn^{4+} \quad \text{vibronic AFM,}$$

$$(5) Fe^{4+} - O^{2-} - Mn^{2+} \quad \text{vibronic AFM.}$$
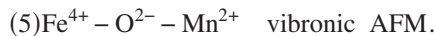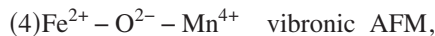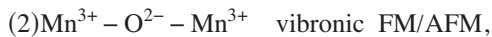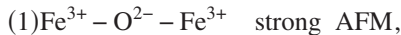
In case (1), both e_g orbitals are half-filled on both sides and present the classic case of correlated antiferromagnetism by virtual charge transfer. Case (2) is less certain because only one $BiFeO_3$ orbital is occupied, thereby producing a weaker AFM. However, if local Jahn-Teller effects become correlated, the AFM ordering can be overcome by a vibronic ferromagnetic (FM) ordering.[25–27] In case (3) for dissimilar cations, a vibronic mechanism is also available, and the most likely result would be a moderate-to-weak antiparallel spin stabilization that is partially offset by delocalization FM exchange between a half-filled and empty pair of overlapping e_g orbital states.

If Fe and Mn are spatially ordered in the B sites, despite an antiparallel alignment a quasi-ferrimagnetic effect could be observed as a net one Bohr magneton moment from the difference between the opposing Fe^{3+} ($S=5/2$) and Mn^{3+}

($S=2$) moments. Cases (4) and (5) are less likely ionic states based on ionization potentials and Madelung energy considerations. The meager Faraday rotation data also indicate that Fe^{3+}/Mn^{3+} ferrimagnetic ordering is not likely since some kind of interionic charge transfer would be necessary to satisfy the $\Delta S = 0$ selection rule for allowed electric dipole transitions.[12,34]

If the specimen is nonstoichiometric, polaronic conduction between mixed-valence cations (double exchange) can create FM properties by any of the following mechanisms (listed according to frequency of occurrence), with effectiveness determined by the particular bonding stabilization and activation energy:

$$(1) Fe^{2+} \leftrightarrow Fe^{3+} + e^- \quad \text{frequent in spinels and garnets,}$$

$$(2) Mn^{3+} \leftrightarrow Mn^{4+} + e^- \quad \text{basis for magnetoresistance in LaSr manganites,}$$

$$(3) Fe^{3+} \leftrightarrow Fe^{4+} + e^- \quad \text{infrequent in spinels and garnets,}$$

$$(4) Mn^{2+} \leftrightarrow Mn^{3+} + e^- \quad \text{infrequent in spinels and garnets.}$$
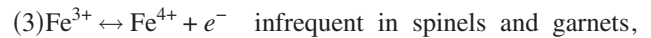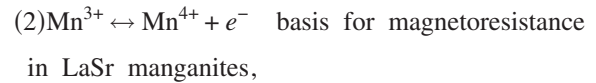
Charges can transport by tunneling at low temperatures or by thermal activation (random hopping) when T approaches the Debye temperature. Note also that static as well as dynamic magnetoelastic effects from Fe^{2+}, Mn^{3+}, or $C2$ can be expected in each situation.

III. EXPERIMENTAL METHODS

$BiFeO_3$ and Bi_2FeMnO_6 thin films were fabricated using pulsed-laser deposition (PLD) with a Coherent COMPexPro 205 KrF (248 nm) excimer laser. The pulse frequency was 10 Hz and the fluence was about 2.5 J/cm^2. $Bi_{1.2}FeO_3$ and $Bi_{2.4}FeMnO_6$ ceramic targets were fabricated by conventional solid-state reaction methods. Before deposition, the chamber was pumped to a vacuum level of 1×10^{-6} torr. By flowing pure O_2, the oxygen partial pressure P_{O_2} was controlled at various levels from 2×10^{-7} torr to 15 mTorr during deposition. MgO and $SrTiO_3$ (STO) single crystals with (001) orientations were used as substrates. During deposition, the substrates were held at various temperatures (T_s) ranging from 530 to 680 °C.

Phase identification was performed using both conventional one-dimensional x-ray diffraction (1DXRD, Rigaku RU300) and two-dimensional x-ray diffraction methods [2DXRD, Bruker D8 with General Area Detector Diffraction System (GADDS)].[35] Element depth profiles of both materials were characterized using a Physical Electronics Model 660 scanning Auger microprobe. Depth profiling was performed using Ar$^+$ ion sputtering over a sample area of 3×3 mm^2. The milling speed was 0.033 nm/s. B-site ion valence states of both films were identified on a Kratos AXIS Ultra imaging x-ray photoelectron spectrometer. The Bi $4f_{7/2}$ peak with binding energy of 158.8 eV was used for energy calibration. Magnetic characterization was performed with vibrating sample magnetometry (VSM) using an ADE Technologies VSM Model 1660. The optical constants (the refrac-

TABLE I. Bi:Fe atomic ratios of BiFeO$_3$ films grown on MgO (001) substrates at various substrate temperatures and oxygen partial pressures.

	530 °C	580 °C	630 °C	680 °C
Vacuum		0.325	0.199	0.230
3 mTorr O$_2$	0.648	0.850	0.800	0.382
7.5 mTorr O$_2$	1.477	0.980	0.961	0.670
15 mTorr O$_2$		1.338	1.307	

tive index n and extinction coefficient k) were characterized from 400 to 1700 nm wavelengths for both films on a WVASE32 ellipsometer. General oscillator models were applied to fit the optical constants, and the fitting root-mean-square error (MSE) was smaller than 1 for both materials. In order to check the validity of the modeling, we also measured transmission spectra for both samples on a Cary 500i UV-Vis-NIR dual-beam spectrophotometer with a range from 175 to 2000 nm. Magneto-optical characterization, i.e., the measurement of Faraday rotation angle as a function of applied magnetic field, was performed at 1550 nm on a custom-built apparatus described in Ref. 36. Composition measurements were performed by wavelength dispersive spectroscopy (WDS).

IV. EXPERIMENTAL RESULTS

A. Element stoichiometry and phase diagram

Table I shows the WDS results for BiFeO$_3$ films grown on MgO (001) substrates at various T_s and P_{O_2}. The bismuth versus iron atomic ratio shows a strong dependence on T_s and P_{O_2} during growth. Near-stoichiometric films can only be achieved in a small process window. Note that either high T_s or low P_{O_2} yield iron-rich films, while either low T_s or high P_{O_2} yield bismuth-rich films. The bismuth deficiency is due to the evaporation of bismuth at high T_s or low P_{O_2}, which is consistent with several previous reports,[15,16,37] and which is partly offset by the use of Bi-rich targets.

The phase diagram of Bi$_2$FeMnO$_6$ as a function of P_{O_2} and T_s during growth is shown in Fig. 1, from data obtained by 2DXRD analysis. For comparison, the results on both STO and MgO substrates are shown. First we notice that
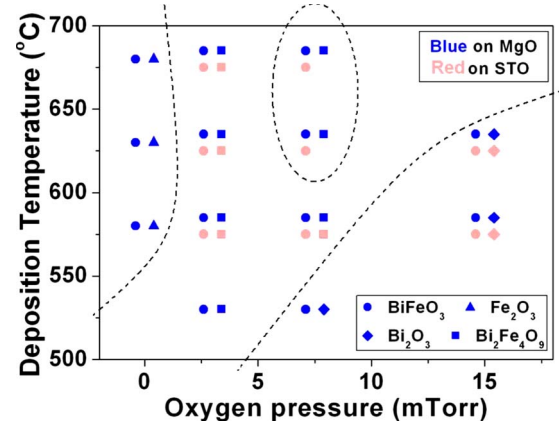
FIG. 1. (Color online) The phases forming during film growth in BiFeO$_3$ deposited on MgO (001) and SrTiO$_3$ (001) substrates as a function of substrate temperature and oxygen partial pressure. The dashed lines separate the conditions under which Fe$_2$O$_3$, Bi$_2$O$_3$ or BiFeO$_3$ perovskite phases dominate. The single-phase perovskite is formed at intermediate pressures and high temperatures on SrTiO$_3$ substrates.

either high T_s or low Bi$_2$FeMnO$_6$ favors the growth of γ-Fe$_2$O$_3$ (maghemite), while either low T_s or high P_{O_2} gives Bi-rich films and favors the growth of Bi$_2$O$_3$. Second, in most of the intermediate temperature and pressure range, BiFeO$_3$ and Mn$_3$O$_4$ coexist on both substrates. On MgO there is no process window for the growth of single-phase perovskite BiFeO$_3$, while on STO, there is a narrow window favoring single-phase BiFeO$_3$ growth, because the BiFeO$_3$ phase is stabilized by epitaxial growth on the STO substrate.[37] Considering the stoichiometry and phase diagram of BiFeO$_3$, it is clear that the atomic ratio of bismuth to iron determines the final phases in the film, and this compositional stoichiometry shows a stronger dependence on P_{O_2} than on T_s. Single phase BiFeO$_3$ films can only be obtained by pseudomorphic growth on a lattice-matched substrate at a P_{O_2} and T_s chosen to give correct film stoichiometry.

Table II shows the phase and compositional analysis of Bi$_2$FeMnO$_6$ films grown on STO substrates. In this system, we fixed T_s at 680 °C and varied P_{O_2} to obtain epitaxial growth of the perovskite phase. Two samples were annealed *in situ* in the PLD chamber for 2 h at the growth conditions before cooling down. The general trend of increasing Bi:(Fe+Mn) with P_{O_2} follows that seen in BiFeO$_3$, but *in*

TABLE II. Phases and compositions of Bi$_2$FeMnO$_6$ films grown on SrTiO$_3$ (001) substrates at 680 °C and various oxygen partial pressures. Two of the samples were *in situ* annealed at the pressure and temperature of the fabrication conditions for 2 h before characterization.

P_{O_2} (mTorr)	Phases	Bi/(Fe+Mn) (at. %)	Fe/Mn (at. %)
0.8	Bi$_2$FeMnO$_6$, γ-Fe$_2$O$_3$, Mn$_3$O$_4$	0.94	0.91
1	Bi$_2$FeMnO$_6$	1.07	0.92
3.5	Bi$_2$FeMnO$_6$, Bi$_2$O$_3$	1.10	0.91
2.5 (*in situ* annealed)	Bi$_2$FeMnO$_6$, Bi$_2$O$_3$, γ-Fe$_2$O$_3$, Mn$_3$O$_4$	0.56	0.95
7.5 (*in situ* annealed)	Bi$_2$FeMnO$_6$, Bi$_2$O$_3$, γ-Fe$_2$O$_3$, Mn$_3$O$_4$	0.65	0.94
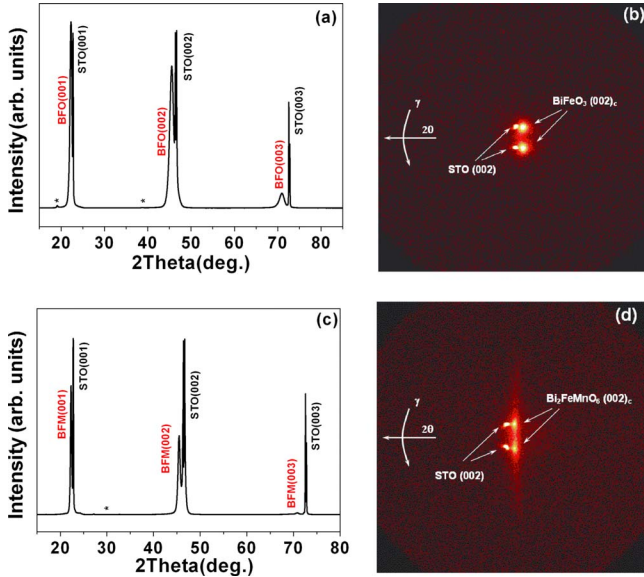
FIG. 2. (Color online) 1DXRD diffraction spectra for (a) $BiFeO_3$ and (c) Bi_2FeMnO_6 epitaxial films on $SrTiO_3$ (001) substrates. "∗" indicates peaks from a trace amount of Bi_2O_3. Also shown are the 2DXRD pseudocubic $(002)_c$ diffraction patterns of (b) $BiFeO_3$ and (d) Bi_2FeMnO_6 films. Both patterns were taken at an x-ray incident angle of $\theta = 23°$ and the frame center was $2\theta = 46°$. The data collection region is $31° \leq 2\theta \leq 61°$ and $75° \leq \gamma \leq 105°$. The samples were rotated by 360° about the axis normal to the sample surface during the measurement.

situ annealing leads to significant loss of Bi and formation of additional Fe and Mn oxides. A single-phase growth window is found around $P_{O_2} = 1$ mTorr for unannealed samples. Compared with $BiFeO_3$ growth, Bi_2FeMnO_6 single-phase growth is more sensitive to fluctuations in fabrication conditions. For example an oxygen pressure change of ± 0.2 mTorr away from 1 mTorr will lead to formation of significant amounts of secondary phases, indicating that Bi_2FeMnO_6 is even less stable than $BiFeO_3$. The Fe:Mn atomic ratio is close to 1 and independent of oxygen pressure.

Based on these results, optimum conditions were chosen to grow epitaxial $BiFeO_3$ and Bi_2FeMnO_6 films with only trace amounts of impurity phases (mainly α-Bi_2O_3 or β-Bi_2O_3) on STO (001) substrates for further analysis. The thickness of the $BiFeO_3$ and Bi_2FeMnO_6 films was 850 and 220 nm, respectively, as confirmed by profilometer. The 1DXRD and 2DXRD spectra of both films are shown in Figs. 2(a)–2(d). Both $BiFeO_3$ and Bi_2FeMnO_6 show $(00k)_c$ pseudocubic diffraction peaks in the 1DXRD spectrum, while the well-defined spotlike diffraction patterns on 2DXRD spectra indicate both films are epitaxially grown on STO. The 1DXRD spectra show that Bi_2FeMnO_6 has a larger out-of-plane lattice parameter than $BiFeO_3$. The in-plane lattice parameter analysis of the (122), (202) and (112) diffraction peaks of both films were carried out by 2DXRD. By fitting the lattice spacing, we obtained all the lattice parameters for both films. $BiFeO_3$ has a monoclinic unit cell with $a = b = 4.037$ Å, $c = 3.947$ Å, and $90° - \beta = -0.88°$, while Bi_2FeMnO_6 has a monoclinic unit cell with $a = 3.915$ Å,
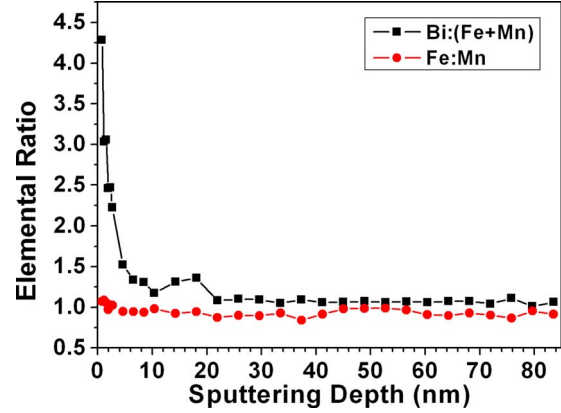
FIG. 3. (Color online) Bi:(Fe+Mn) and Fe:Mn atomic ratios in a Bi_2FeMnO_6 film as a function of depth, from Auger electron spectroscopy.

$b = 3.935$ Å, $c = 3.986$ Å and $90° - \beta = -0.5°$, where β is the angle between the a and b directions. Both films are distorted to monoclinic symmetry with c axis out-of-plane by their epitaxial relation with the substrate. Bi_2FeMnO_6 shows a smaller unit-cell volume (61.40 Å^3) compared with $BiFeO_3$ (64.31 Å^3). Compared with the $SrTiO_3$ substrate (cubic cell with $a = 3.905$ Å and unit-cell volume 59.55 Å^3), the largest in-plane lattice mismatch of $BiFeO_3$ and Bi_2FeMnO_6 are 3.4% and 0.8%, respectively. Although better lattice matching is achieved in Bi_2FeMnO_6, the film quality is not as good as for $BiFeO_3$. At a Bi_2FeMnO_6 thickness of 220 nm, a small amount of impurity phase is observed, and this increases with thickness. In contrast, for $BiFeO_3$, epitaxial film growth was achieved at a thickness of 850 nm, and the impurity phase was limited to a trace amount. This observation suggests that the perovskite phase of Bi_2FeMnO_6 is less stable compared with $BiFeO_3$.

B. Element depth profile and valence states

Auger electron spectroscopy (AES) was carried out to measure the element depth profile of both samples. Figure 3 shows the result on the Bi_2FeMnO_6 film. The Bi:(Fe+Mn) atomic ratio is 4.5 at the film surface but decreases to 1 within 10 nm film thickness, while the Fe:Mn atomic ratio remains almost constant. There is no change in either ratio for the remaining thickness of the film. This surface bismuth-rich layer is also found in the $BiFeO_3$ film according to AES and XPS surface analysis. However, due to large charging effects in this film, we could not obtain a clear AES depth profile spectrum. The bismuth-rich surface layer was found previously in epitaxial $BiFeO_3$ films and was attributed to strain relaxation along the thickness direction of the film.[37] This effect causes the $BiFeO_3$ phase to have a higher free energy of formation than Bi_2O_3 near the film surface, favoring the growth of the latter.

Figures 4(a)–4(c) show the XPS core level spectra of Fe 2p in $BiFeO_3$, and Fe 2p and Mn 2p in Bi_2FeMnO_6, respectively. To assure our analysis was carried out on the perovskite phase, Ar$^+$ ion milling was performed until the bismuth concentration was stable in survey scans. The XPS
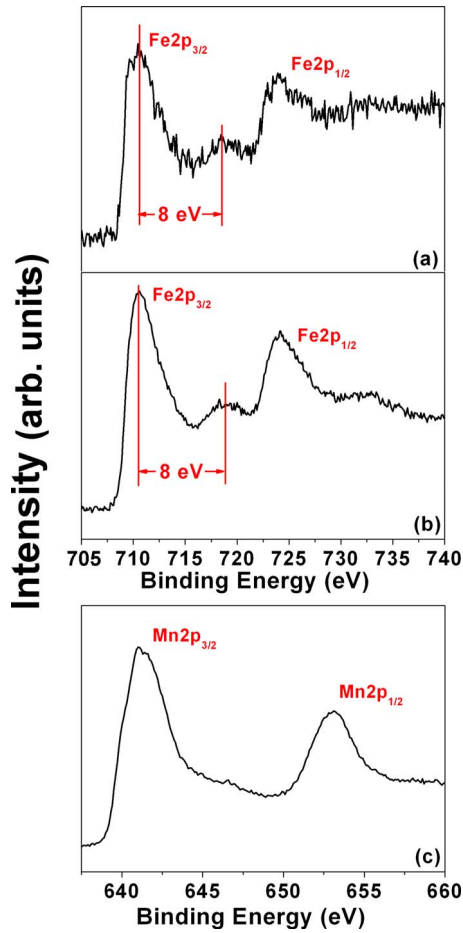
FIG. 4. (Color online) XPS spectra of the Fe $2p$ peaks for (a) $BiFeO_3$ and (b) Bi_2FeMnO_6 and (c) the Mn $2p$ peaks for Bi_2FeMnO_6.

FIG. 5. (Color online) (a) Magnetization as a function of out-of-plane applied field for $BiFeO_3$ and Bi_2FeMnO_6 films at room temperature. (b) In-plane magnetization of a Bi_2FeMnO_6 film measured by SQUID magnetometry at 5 K. The plot shows a half loop scanning from -9000 to 9000 Oe.

spectra of Fe and Mn reveal the usual $2p_{3/2}$ and $2p_{1/2}$ doublet arising from spin-orbital interaction. Comparing both spectra we found that the Fe $2p$ lines resemble each other in $BiFeO_3$ and Bi_2FeMnO_6 films. The binding energy of the Fe $2p_{3/2}$ level is 710.57 eV in $BiFeO_3$ and 710.61 eV in Bi_2FeMnO_6. No shoulder peak was found around the Fe $2p_{3/2}$ peak in either sample. Moreover, a satellite peak was found about 8.0 eV above the Fe $2p_{3/2}$ principal peak. This satellite peak is considered to be characteristic of the oxidation state of the Fe.[29] Due to different d orbital electron configurations, during relaxation of the metal ions, Fe^{2+} and Fe^{3+} will show a satellite peak at 6 eV or 8 eV above their $2p_{3/2}$ principal peaks, respectively.[38] The structure and similarity of the Fe $2p$ core level spectra in both $BiFeO_3$ and Bi_2FeMnO_6 films indicate that Fe is mainly in the 3+ valence state in both systems. On the other hand, in the Bi_2FeMnO_6 film, the Mn $2p_{3/2}$ principal peak has a binding energy of 642.2 eV. A shoulder peak below this energy originates from Mn^{2+} and indicates the presence of multiple valence states of Mn. In the stoichiometric Bi_2FeMnO_6, the average valence state of the B-site cation is 3+, and since Fe is mainly present as 3.75 μ_B, this suggests that Mn must exhibit Mn^{2+}, Mn^{3+}, and Mn^{4+} valence states. Previous XPS analysis on 10 at. % Mn-doped $BiFeO_3$ indicates that the oxidation state of Fe

was primarily 3+.[29] From our analysis this effect seems to persist even with 50 at. % Mn present in the B sites.

C. Magnetic and magneto-optical properties

Figure 5(a) shows the out-of-plane magnetic hysteresis loops of $BiFeO_3$ and Bi_2FeMnO_6 films measured at room temperature by VSM. The data were obtained by subtracting the substrate magnetization from the overall hysteresis of the samples. Both samples show low and nonsaturating magnetization for an applied magnetic field up to 10 kOe. $BiFeO_3$ exhibits a magnetization of 1.2 emu/cm³ at 1 kOe resulting from slight canting of the antiferromagnetically-coupled moments, while Bi_2FeMnO_6 exhibits an even smaller magnetization of 0.8 emu/cm³. These results suggest that the magnetization in Bi_2FeMnO_6 also originates from canted antiferromagnetism at room temperature. In order to investigate the magnetic ordering of Bi_2FeMnO_6 at low temperatures, we measured the magnetization of Bi_2FeMnO_6 at 5 K using a superconducting quantum interference device (SQUID) magnetometer, as shown in Fig. 5(b). Bi_2FeMnO_6 shows nonsaturating behavior at this temperature. The magnetization at 9 kOe is estimated at 5.4 emu/cm³, corresponding to 0.03 μ_B per B-site ion. This value is far from the values expected if the Fe and Mn atoms were ordered in the B sites (4 μ_B for ferromagnetic or 0.5 μ_B for antiferromagnetic ordering of Fe^{3+} and Mn^{3+}), which indicates most of the B-site cations are disordered in this sample.

Faraday rotation hysteresis loops of both films at a wavelength of 1550 nm at room temperature were also measured on both samples. Due to the very low magnetization of both samples, no clear hysteresis was obtained. By subtracting the Faraday rotation signal from our substrate, we estimated the Verdet constant (Faraday rotation per unit length, per unit field strength for light traveling along the applied magnetic field direction in a magneto-optical medium) for both films. $BiFeO_3$ shows a Verdet constant of $18 \pm 2 °/$cm kOe, while Bi_2FeMnO_6 shows a Verdet constant of $50 \pm 3 °/$cm kOe.

D. Optical properties

Figure 6(a) shows the fitted optical constants for the $BiFeO_3$ film as a function of wavelength. At 1550 nm wavelength, the refractive index is $n=2.592$ and k is smaller than the detection error of the equipment. The small extinction
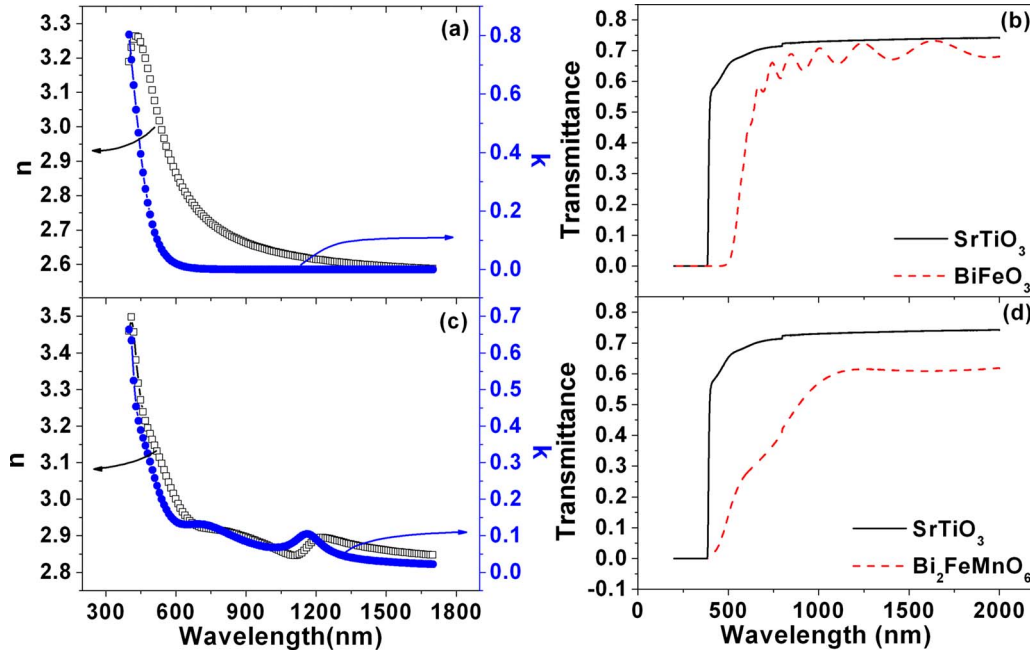
FIG. 6. (Color online) Optical constants as a function of wavelength for (a) $BiFeO_3$ and (c) Bi_2FeMnO_6 films as measured by ellipsometry; incident light transmittance as a function of wavelength for (b) $BiFeO_3$ and (d) Bi_2FeMnO_6 films as measured by spectrophotometry.

coefficient indicates $BiFeO_3$ is very transparent, similar to yttrium and other rare-earth orthoferrites in the infrared wavelength region.[32,33] The validity of our fitting is supported by comparing the n, k data with the spectrophotometry absorption spectra shown in Fig. 6(b). First, the optical band gaps of $BiFeO_3$ measured by both methods are very similar. If one estimates the band gap of $BiFeO_3$ by the photon energies at the optical absorption edge, the measured band gap for $BiFeO_3$ is 2.44 eV by ellipsometry and 2.42 eV by spectrophotometry. Second, using the fitted film thickness, the n, k data and the substrate optical constants, we can obtain a good fit to the experimental absorption spectrum. Note that our fitting did not include the absorption peaks located around 1.0 and 0.7 μm caused by Fe^{3+} $^6A_1 \rightarrow {}^4T_1$ and $^6A_1 \rightarrow {}^4T_2$ crystal-field transitions, which will result in underestimation of the extinction coefficient around these wavelengths. But from both the results of ellipsometry and spectrophotometry, it is clear that $BiFeO_3$ has low optical absorption loss at 1550 nm wavelength.

Figure 6(c) shows the fitted optical constants for the Bi_2FeMnO_6 film as a function of wavelength. Quite different from $BiFeO_3$, this film shows a refractive index of $n=2.85$ and an extinction coefficient of $k=0.048$ at 1550 nm wavelength. We modeled both the surface layer and the underlying Bi_2FeMnO_6 film in this case, because the Bi-rich surface layer thickness is not negligible compared with the overall thickness of this sample. Also, an absorption peak is clear around 1100 nm wavelength. The high extinction coefficient of Bi_2FeMnO_6 film is confirmed by the spectrophotometer results shown in Fig. 6(d). The Bi_2FeMnO_6 sample has a much lower transmittance in the infrared region compared with the bare STO substrate.

V. FIRST-PRINCIPLES METHODS AND RESULTS

The difficulty in analyzing a multi-cation system wherein the distribution of magnetic ions is neither rigorously or-

dered nor random (likely the case for Fe and Mn in Bi_2FeMnO_6) is compounded by the occurrence of variable valence states among the B-site cations. Regrettably, a semi-empirical "mean" field solution often becomes the best option. In this case, however, where there is no magnetic dilution of the B lattice, band theory computations might clarify the homogeneity question and serve as a bridge between the local expectations and a molecular field approach. In order to understand the structure, electronic structure, and magnetic properties of $BiFeO_3$ and Bi_2FeMnO_6, we therefore applied density-functional theory with spin polarized generalized gradient approximation (GGA) and GGA$+U$ (Liechtenstein's implementation)[39] methods to calculate the structure and electronic structure of both materials. Projected augmented wave (PAW)[40] pseudopotentials are used, as implemented in the vienna *ab initio* simulation package (VASP).[41] The cut-off energy was 500 eV. $5 \times 5 \times 5$, $3 \times 3 \times 3$ and $3 \times 3 \times 3$ k-point meshes were used for $BiFeO_3$, $BiMnO_3$ and Bi_2FeMnO_6, respectively. Full relaxation of the atomic coordinates and lattice vectors was achieved using both GGA and GGA$+U$ energy functionals until the total ground-state energies converged within 3 meV for each unit cell. The screened Coulomb interaction parameter U and exchange parameter J enter the Hamiltonian to account for the on-site electron-electron interactions in the localized 3d orbitals for Fe and Mn. In this work, we set $U=J=0$ eV for GGA calculations. For GGA$+U$ calculations, we fixed J(Fe) $=J$(Mn)$=1$ eV, and varied U(Fe) or U(Mn) from 4 to 8 eV.

We assumed the space group for $BiFeO_3$ and $BiMnO_3$ to be $R3c$ and $C2$, respectively, according to experimental results,[15,22] while we varied the space groups for Bi_2FeMnO_6 unit cell to be $Pm\bar{3}m$, $R3$, and $C2$. The magnetic configurations for $BiFeO_3$ and $BiMnO_3$ were set to be G-AFM and FM, respectively. For Bi_2FeMnO_6, both FM and G-AFM configurations are presumed for each structural symmetry. In

TABLE III. Calculated lattice parameters of $BiFeO_3$ (space group $R3c$), $BiMnO_3$ (space group $C2$), and Bi_2FeMnO_6 (space groups $Pm\bar{3}m$, $R3$, and $C2$) calculated using the GGA+U method. Also shown is the formation enthalpy of Bi_2FeMnO_6. G-AFM and FM magnetic ordering were assumed for $BiFeO_3$ and $BiMnO_3$, respectively. Both FM and G-AFM ordering were assumed for Bi_2FeMnO_6. $U(Fe)=7$ eV, $J(Fe)=1$ eV, $U(Mn)=6$ eV, and $J(Mn)=1$ eV were used for all calculations.

	$BiFeO_3$	$BiMnO_3$	Bi_2FeMnO_6				
Space group	$R3c$	$C2$	$Pm\bar{3}m$		$R3$	$C2$	
Magnetic ordering	G-AFM	FM	FM	G-AFM	FM	FM	G-AFM
$a(\text{Å})$	5.67	9.71	7.86	7.84	5.71	9.50	9.50
$b(\text{Å})$	5.67	5.70	7.86	7.84	5.71	5.80	5.77
$c(\text{Å})$	5.67	10.00	7.86	7.84	5.71	9.78	9.76
$\alpha(°)$	59.11	90	90	90	59.15	90	90
$\beta(°)$	59.11	111.11	90	90	59.15	107.91	107.91
$\gamma(°)$	59.11	90	90	90	59.15	90	90
$\Omega(\text{Å}^3)$	126.28	516.33	485.83	482.04	129.09	512.74	508.91
Formation enthalpy per Bi basis (eV)	N/A	N/A	1.162	1.155	0.203	0.092	0.057

order to investigate how Mn valence state influences the unit-cell structure, we also varied Mn to be Mn^{2+}, Mn^{3+}, and Mn^{4+} by starting with different spin configurations on the Mn atoms. As a consequence, Fe was set to be Fe^{4+}, Fe^{3+}, Fe^{2+}, respectively in these configurations. To estimate the formation enthalpy of Bi_2FeMnO_6, we considered the following reaction at 0 K temperature:

$$BiFeO_3 + BiMnO_3 \rightarrow Bi_2FeMnO_6.$$
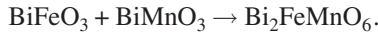
The formation enthalpy of Bi_2FeMnO_6 was estimated as

$$\Delta H_f = E(Bi_2FeMnO_6) - E(BiFeO_3) - E(BiMnO_3),$$

where E is the total energy after structure relaxation. By fixing $BiFeO_3$ and $BiMnO_3$ in the $R3c$ and $C2$ space groups, respectively, we can compare the formation enthalpy of Bi_2FeMnO_6 with different symmetries. Note that we neglect the small $P\Delta V$ term. This is applicable for reactions at atmosphere pressure, but it is not applicable for reactions carried out at high pressures such as several GPa.

A. Structure and formation enthalpy

Table III shows the structural parameters of $BiFeO_3$, $BiMnO_3$, and Bi_2FeMnO_6 and the formation enthalpy of Bi_2FeMnO_6 after unit-cell relaxation. We fixed $U(Fe)$ $=7$ eV and $U(Mn)=6$ eV for all related calculations. The calculated $BiFeO_3$ and $BiMnO_3$ lattice parameters show good agreement with experimental data.[42,43] For Bi_2FeMnO_6 there are three noticeable features in the calculation results. First of all, the formation enthalpy of Bi_2FeMnO_6 is always positive for all the structures and magnetic orderings we examined, suggesting that B-site ordered Bi_2FeMnO_6 is unstable at 0 K. The positive formation enthalpy comes from the Fe and Mn octahedrons as nearest neighbors. Thus, checkerboard-type B-site ordering is thermodynamically unfavored. Second, both the unit-cell structure and magnetic ordering affect the formation enthalpy of Bi_2FeMnO_6, with the former having the larger influence. The most stable struc-

ture of Bi_2FeMnO_6 is monoclinic with $C2$ space group. This result is not hard to interpret if one compares Bi_2FeMnO_6 with the lattice structure of $BiMnO_3$. In both systems Mn stays at the 3+ valence state, which creates a large lattice distortion due to the Jahn-Teller effect. This distortion is uniaxial, which distorts the unit cell from cubic to tetragonal. Meanwhile, the $6s^2$ lone pair states on Bi^{3+} ions further distort the unit cell to a noncentrosymmetric structure.[9] Note that we cannot obtain stable antiferromagnetic spin ordering during lattice relaxation in Bi_2FeMnO_6 with $R3$ symmetry. Third, by comparing the formation enthalpy of Bi_2FeMnO_6 with FM and AFM magnetic ordering, one finds that AFM ordering is more stable for Bi_2FeMnO_6 with both $Pm\bar{3}m$ and $C2$ symmetries.

In order to verify the effect of cation valence state, we fixed the unit cell of Bi_2FeMnO_6 with $C2$ symmetry and varied the Mn valence states between Mn^{2+}, Mn^{3+}, and Mn^{4+}. As a consequence, Fe is set as Fe^{4+}, Fe^{3+}, and Fe^{2+}, respectively. Fe and Mn are antiferromagnetically coupled in these calculations. However, after lattice relaxation, all three cases relax to a Fe^{3+}/Mn^{3+} configuration, indicating this configuration is thermodynamically most stable. This result is consistent with our XPS measurement that both Fe and Mn ions are mostly in the 3+ valence state. However, experimentally we observed small amount of Mn^{2+} and Mn^{4+} in our films. One possible explanation may be related to the behavior of Mn^{3+} (high spin, hs) which is a Jahn-Teller ion and which distorts the unit cell to larger sizes.[9] If multiple valence states of Mn are present, the film can decrease the lattice distortion that would be caused by Mn^{3+} alone, which may result in better lattice matching between the film and the substrate. Other possibilities such as film defects may also have played an important role in changing the valence states of Mn.

B. Electronic structures and effect of U

To investigate the electronic structure of $BiFeO_3$, $BiMnO_3$ and Bi_2FeMnO_6, we also carried out calculations on the den-
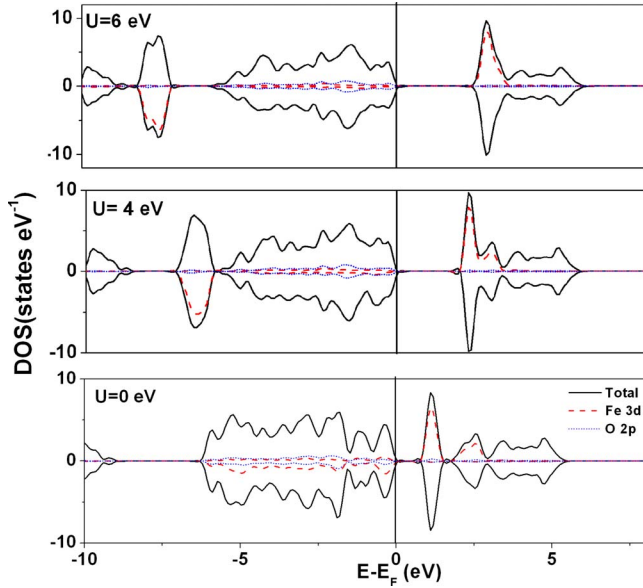
FIG. 7. (Color online) Total, Fe $3d$ and O $2p$ DOS for $R3c$-structured BiFeO$_3$ calculated using GGA method ($U=J=0$ eV) and GGA$+U$ method ($J=1$ eV, $U=5$ eV and $J=1$ eV $U=7$ eV). The total DOS is normalized to a formula unit of Bi$_2$Fe$_2$O$_6$. As U increases, the calculated band-gap energy increases, and the ionicity of Fe-O bonds increases.

FIG. 8. (Color online) Total, Fe $3d$ and O $2p$ DOS for $C2$ BiMnO$_3$ calculated using GGA method ($U=J=0$ eV) and GGA$+U$ method ($J=1$ eV, $U=6$ eV and $J=1$ eV, $U=8$ eV). The total DOS is normalized to a formula unit of Bi$_2$Mn$_2$O$_6$.

sity of states (DOS) of these compounds. Figure 7 shows the calculated DOS for both spin channels of $R3c$ BiFeO$_3$ using various U values. In all three calculations, BiFeO$_3$ is predicted to be an insulator. The band gaps are 0.4 eV, 2 eV and 2.4 eV for $U=0$ eV, 5 eV and 7 eV, respectively. Increasing the U value significantly increases the band gap, and $U=7$ eV shows the band-gap value closest to our experimental values. Changing the U value also influences the ionicity of the Fe-O bonding. For $U=0$ eV, Fe $3d$ and O $2p$ valence electrons show strong hybridization in the energy range of -6 to 0 eV, indicating the Fe-O bonding is highly covalent. This is not reasonable if we consider the electronegativity is quite different between Fe (1.83) and O (3.44). However, as the U value increases, Fe $3d$ valence electrons are pushed down to lower energy levels, and the $t_{2g}-e_g$ energy split is smaller. This indicates that the Fe-O bonding is more ionic and the electrons are more localized on the Fe and O atoms. Electron spin integration around the Fe site shows that the magnetic moment of Fe is 3.75 μ_B, 4.13 μ_B and 4.25 μ_B for $U=0$ eV, 5 eV and 7 eV, respectively. Interestingly, $U=0$ eV rather than $U=7$ eV provides the best prediction of Fe magnetic moment compared with experiments.[44] These calculation results using the GGA$+U$ method are similar to previous results calculated by local spin-density approximation (LSDA) and LSDA$+U$ methods.[17] The difference is that for the same U value, GGA predicts slightly larger band gaps and Fe magnetic moments compared with LSDA.

Figure 8 shows the calculated DOS of $C2$ BiMnO$_3$ for both spin channels using the GGA$+U$ method ($U=0$, 6, and 8 eV). For insulating BiMnO$_3$, it is well known that the LSDA method predicts a half-metallic band structure.[9,45,46] This is due to the strong hybridization tendency between Mn $3d$ and O $2p$ orbitals in first-principles calculations. Our
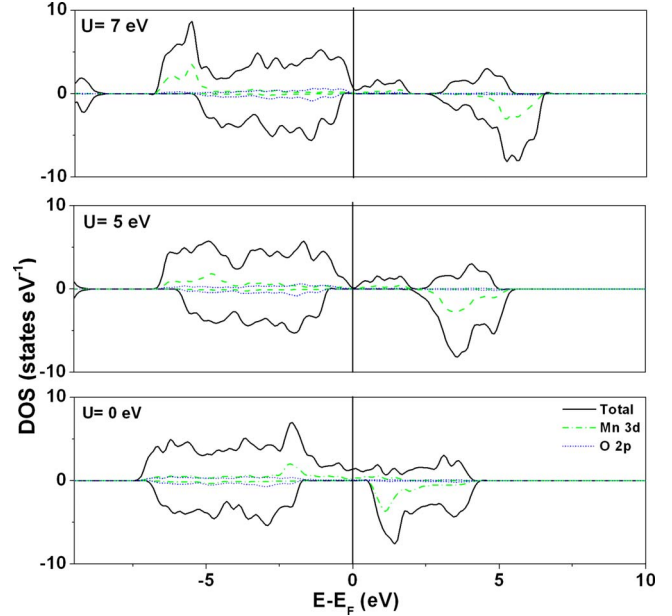
calculation based on monoclinic BiMnO$_3$ using the GGA method also shows similar behavior. When $U=0$ eV, Mn $3d$ and O $2p$ electrons strongly hybridize and there is no band gap. Applying the GGA$+U$ method enhances the ionicity of the Mn-O bonding and creates a dip in the DOS near the Fermi energy level. A gap of about 0.4 eV opens between the occupied and unoccupied Mn $e_g^{\uparrow}$ states. This effect was observed by Shishidou *et al.*[46] using LDA$+U$ calculations. Unlike BiFeO$_3$, as we increase the U value up to 8 eV, this gap does not increase.

However, applying GGA or GGA$+U$ methods to calculate the electronic structure of $C2$ Bi$_2$FeMnO$_6$ shows dramatic differences compared with BiMnO$_3$. Figures 9(a) and 9(b) show the calculated DOS of monoclinic Bi$_2$FeMnO$_6$ with antiferromagnetic spin ordering by applying GGA and GGA$+U$ methods (U(Fe)$=7$ eV, U(Mn)$=6$ eV), respectively. The GGA method predicts Bi$_2$FeMnO$_6$ to be half metallic, while GGA$+U$ indicates Bi$_2$FeMnO$_6$ should be insulating. Compared with our optical measurements, it is clear that the GGA$+U$ method provides a more realistic result. Looking closely into the details of the density of states, the 100% spin polarized structure in the GGA calculation is due to the hybridization of Fe $3d$, O $2p$, and Mn $3d$ orbitals. The unoccupied Mn $e_g^{\downarrow}$ states hybridize with Fe $t_{2g}^{\downarrow}$ and $e_g^{\downarrow}$ states through oxygen, causing a half-metallic structure. In the GGA$+U$ method, the Coulomb repulsion and correlation interaction correction causes lower hybridization between Fe and Mn orbitals, and a gap opens above the Fermi level. Despite this, hybridized states among Fe $3d$, Mn $3d$, and O $2p$ orbitals can still be found in the valence and conduction bands. This result predicts that Mn-O-Fe type hopping conduction is likely to take place in Bi$_2$FeMnO$_6$.
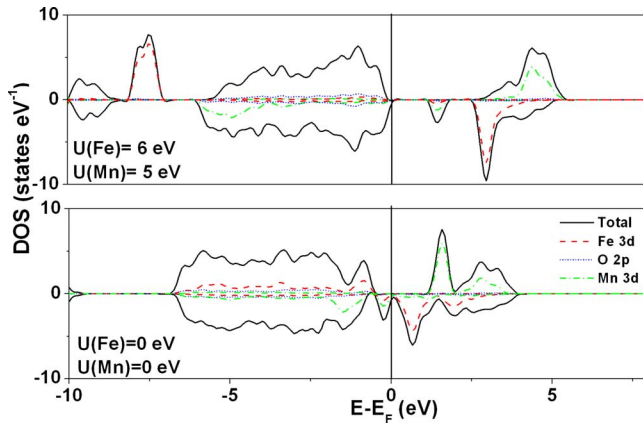
FIG. 9. (Color online) Total, Fe 3d and O 2p DOS for $C2$ Bi$_2$FeMnO$_6$ calculated using GGA method (J(Fe)=J(Mn)=0 eV, U(Fe)=U(Mn)=0 eV) and GGA+U method (J(Fe)=1 eV, U(Fe)=7 eV and J(Mn)=1 eV, U(Mn)=6 eV). The total DOS is normalized to a formula unit of Bi$_2$FeMnO$_6$. The GGA method predicts a half-metallic band structure while GGA+U indicates this material should be insulating.

VI. DISCUSSION

It is now useful to compare our experimental results and calculations to understand the properties of Bi$_2$FeMnO$_6$. The formation enthalpy for bulk ordered Bi$_2$FeMnO$_6$ is predicted to be positive for several crystal symmetries by density-functional theory, which assumes equilibrium phases and atmospheric pressure. This suggests that neighboring Fe and Mn octahedra are not thermodynamically favored in this material; thus it could be difficult to fabricate it as an ordered bulk material. This observation is evident in one previous study by Yang *et al.*,[47] who claimed that incorporating Mn >30 at. % on the B site of BiFeO$_3$ is difficult unless high pressure processing is used. Experimentally, the smaller process window for forming Bi$_2$FeMnO$_6$ as compared to BiFeO$_3$ (the oxygen pressure window for BiFeO$_3$ growth exceeds 4.5 mTorr while for Bi$_2$FeMnO$_6$ it is smaller than 0.4 mTorr) may be indicative of the relative instability of the Bi$_2$FeMnO$_6$ perovskite phase, and our films showed no evidence of B-site ordering. In contrast, there are several ordered double perovskites that can be grown by bulk processing, such as La$_2$MnNiO$_6$,[48] La$_2$MnCoO$_6$,[49] and Sr$_2$FeMoO$_6$,[50] and it will be interesting to investigate whether a negative formation enthalpy is predicted in these ordered perovskites following the computational methods used here.

We observed experimentally that Mn tends to adopt multiple valence states in the perovskite film. From the calculation results we infer that Mn^{3+} is thermodynamically the most stable ion in Bi$_2$FeMnO$_6$. One possible explanation of the experimental observation is that by Mn adopting multivalence states, the material can reduce the Jahn-Teller effect from Mn^{3+}. For a thin-film material, this process may pro-

mote better lattice matching with the substrate, lowering the interface and strain energies. Other factors such as film defects may also affect the valence states of Mn.

In Bi$_2$FeMnO$_6$, the electronic structure calculation predicts a strong tendency for Fe-O-Mn hybridization, and the resulting conductivity due to interatomic hopping is expected to be higher than the conductivity of BiFeO$_3$. The optical absorption spectrum may provide some insight into the conductivity. The large absorption of Bi$_2$FeMnO$_6$ in the infrared may be due to free-carrier absorption. The absorption peak around 1100 nm does not correspond to any dipole transition energies of Fe or Mn sites, and may therefore be due to interatomic electron hopping, i.e., Verwey conduction. In addition, hopping conduction between Mn with different valence states is possible, as observed for example in La$_{1-x}$Sr$_x$MnO$_3$ perovskite.[51] This requires significant amounts of Mn^{2+} and Mn^{4+} to allow percolation to take place. Quantitative analysis on the amount of Mn^{2+} and Mn^{4+} ions may provide more information on the importance of these two conduction mechanisms. The relatively high conductivity of polycrystalline Bi$_2$FeMnO$_6$ was shown in one previous study, although grain-boundary conduction and the effects of secondary phases may have been important.[52]

VII. CONCLUSIONS

The structure, magnetic, and magneto-optical properties of BiFeO$_3$ and Bi$_2$FeMnO$_6$ have been investigated using both experimental and first-principles methods. Both BiFeO$_3$ and Bi$_2$FeMnO$_6$ can be epitaxially grown in the perovskite structure on SrTiO$_3$ (001) substrates within a small window of process parameters. Compared with BiFeO$_3$, Bi$_2$FeMnO$_6$ shows a smaller process window, and its magnetic properties imply that the B-site cations are disordered. These observations are attributed to the positive formation enthalpy of ordered Bi$_2$FeMnO$_6$ compared with BiFeO$_3$ and BiMnO$_3$ at 0 K. Mn tends to form multiple valence states in Bi$_2$FeMnO$_6$ despite the higher stability of the compound only containing Mn^{3+} ions, possibly because the incorporation of Mn^{2+} or Mn^{4+} decreases the Jahn-Teller effect of Mn^{3+} in the film. Bi$_2$FeMnO$_6$ had a large optical absorption compared to BiMnO$_3$ as a result of electron hopping between Fe and Mn sites as well as between Mn sites with different valence states. These studies provide a comparison between the structure and properties of BiFeO$_3$ perovskite and Bi$_2$FeMnO$_6$ double perovskite which may be applicable to other perovskite and multiferroic systems.

*Also at MIT Lincoln Laboratory Lexington, Massachusetts, 02420.

[1] P. Baettig, C. Ederer, and N. A. Spaldin, Phys. Rev. B **72**, 214105 (2005).

[2] M. Azuma, K. Takata, T. Saito, S. Ishiwata, Y. Shimawaka, and M. Takano, J. Am. Chem. Soc. **127**, 8889 (2005).

[3] R. Nechache, C. Harnage, A. Pignolet, F. Normandin, T. Veres, L. Carignan, and D. Ménard, Appl. Phys. Lett. **89**, 102902 (2006).

[4] X. Tan, R. Wongmaneerung, and R. W. McCallum, J. Appl. Phys. **102**, 104114 (2007).

[5] S. Yasui, H. Uchida, H. Nakaki, K. Nishida, H. Funakubo, and S. Koda, Appl. Phys. Lett. **91**, 022906 (2007).

[6] N. A. Hill, J. Phys. Chem. B **104**, 6694 (2000).

[7] G. A. Smolenskii and I. Chupis, Sov. Phys. Usp. **25**, 475 (1982).

[8] N. A. Spaldin and M. Fiebig, Science **309**, 391 (2005).

[9] R. Seshadri and N. A. Hill, Chem. Mater. **13**, 2892 (2001).

[10] M. Levy, IEEE J. Sel. Top. Quantum Electron. **8**, 1300 (2002).

[11] D. C. Hutchings, J. Phys. D **36**, 2222 (2003).

[12] G. F. Dionne, A. R. Taussig, M. Bolduc, L. Bi, and C. A. Ross, J. Appl. Phys. **101**, 09C524 (2007).

[13] G. F. Dionne and G. A. Allen, J. Appl. Phys. **73**, 6127 (1993).

[14] G. F. Dionne and G. A. Allen, J. Appl. Phys. **75**, 6372 (1994).

[15] H. Bea, M. Bibes, A. Barthelemy, K. Bouzehouane, E. Jacquet, A. Khodan, J.-P. Contour, S. Fusil, F. Wyczisk, A. Forget, D. Lebeugle, D. Colson, and M. Viret, Appl. Phys. Lett. **87**, 072508 (2005).

[16] J. Li, J. Wang, M. Wuttig, R. Ramesh, N. Wang, B. Ruette, A. P. Pyatakov, A. K. Zvezdin, and D. Viehland, Appl. Phys. Lett. **84**, 5261 (2004).

[17] J. B. Neaton, C. Ederer, U. V. Waghmare, N. A. Spaldin, and K. M. Rabe, Phys. Rev. B **71**, 014113 (2005).

[18] J. Wang, Ph.D. thesis, University of Maryland, 2005.

[19] S. V. Kiselev, R. P. Ozerov, and G. S. Zhdanov, Sov. Phys. Dokl. **7**, 742 (1963).

[20] J. R. Teague, R. Gerson, and W. J. James, Solid State Commun. **8**, 1073 (1970).

[21] B. Ruette, S. Zvyagin, A. P. Pyatakov, A. Bush, J. F. Li, V. I. Belotelov, A. K. Zvezdin, and D. Viehland, Phys. Rev. B **69**, 064114 (2004).

[22] A. Sharan, J. Lettieri, Y. Jia, W. Tian, X. Pan, D. G. Schlom, and V. Gopalan, Phys. Rev. B **69**, 214109 (2004).

[23] T. Kimura, S. Kawamoto, I. Yamada, M. Azuma, M. Takano, and Y. Tokura, Phys. Rev. B **67**, 180401(R) (2003).

[24] A. Moreira dos Santos, S. Parashar, A. R. Raju, Y. S. Zhao, A. K. Cheetham, and C. N. R. Rao, Solid State Commun. **122**, 49 (2002).

[25] J. B. Goodenough, *Magnetism and the Chemical Bond* (Wiley, New York, 1963), Table XII.

[26] J. B. Goodenough, A. Wold, N. Menyuk, and R. J. Arnott, Phys. Rev. **124**, 373 (1961).

[27] G. F. Dionne, J. Appl. Phys. **79**, 5172 (1996).

[28] C. H. Yang, J. H. Song, H. J. Lee, S. Yoon, T. Y. Koo, and Y. H. Jeong, Phys. Status Solidi B **241**, 1453 (2004).

[29] D. Kothari, V. R. Reddy, A. Gupta, D. M. Phase, N. Lakshmi, S. K. Deshpande, and A. M. Awasthi, J. Phys.: Condens. Matter **19**, 136202 (2007).

[30] J. R. Sahu and C. N. R. Rao, Solid State Sci. **9**, 950 (2007).

[31] V. R. Palkar, D. C. Kundaliya, and S. K. Malik, J. Appl. Phys. **93**, 4337 (2003).

[32] D. L. Wood, J. P. Remeika, and E. D. Kolb, J. Appl. Phys. **41**, 13 (1970).

[33] W. J. Tabor, A. W. Anderson, and L. G. Van Uitert, J. Appl. Phys. **41**, 3018 (1970).

[34] G. F. Dionne and G. A. Allen, J. Appl. Phys. **95**, 7333 (2004).

[35] B. B. He, Powder Diffr. **18**, 71 (2003).

[36] A. Rajamani, G. F. Dionne, D. Bono, and C. A. Ross, J. Appl. Phys. **98**, 063907 (2005).

[37] H. Béa, M. Bibes, S. Fusil, K. Bouzehouane, E. Jacquet, K. Rode, P. Bencok, and A. Barthélémy, Phys. Rev. B **74**, 020101(R) (2006).

[38] C. Wandelt, Surf. Sci. Rep. **2**, 1 (1982).

[39] A. I. Liechtenstein, V. I. Anisimov, and J. Zaanen, Phys. Rev. B **52**, R5467 (1995).

[40] G. Kresse and D. Joubert, Phys. Rev. B **59**, 1758 (1999).

[41] G. Kresse and J. Furthmüller, Phys. Rev. B **54**, 11169 (1996).

[42] F. Kubel and H. Schmid, Acta Crystallogr., Sect. B: Struct. Sci. **46**, 698 (1990).

[43] T. Atou, H. Chiba, K. Ohoyama, Y. Yamaguchi, and Y. Syono, J. Solid State Chem. **145**, 639 (1999).

[44] I. Sosnowska, W. Schäfer, W. Kockelmann, K. H. Andersen, and I. O. Troyanchuk, Appl. Phys. A: Mater. Sci. Process. **74**, S1040 (2002).

[45] N. A. Hill and K. M. Rabe, Phys. Rev. B **59**, 8759 (1999).

[46] T. Shishidou, N. Mikamo, Y. Uratani, F. Ishii, and T. Oguchil, J. Phys.: Condens. Matter **16**, S5677 (2004).

[47] C. H. Yang, T. Y. Koo, and Y. H. Jeong, Solid State Commun. **134**, 299 (2005).

[48] N. S. Rogado, J. Li, A. W. Sleight, and M. A. Subramanian, Adv. Mater. (Weinheim, Ger.) **17**, 2225 (2005).

[49] C. L. Bull, D. Gleeson, and K. S. Knight, J. Phys.: Condens. Matter **15**, 4927 (2003).

[50] K. I. Kobayashi, T. Kimura, H. Sawada, K. Terakura, and Y. Tokura, Nature (London) **395**, 677 (1998).

[51] M. Izumi, T. Manako, Y. Konishi, M. Kawasaki, and Y. Tokura, Phys. Rev. B **61**, 12187 (2000).

[52] S. K. Singh, H. Ishiwara, and K. Maruyama, Appl. Phys. Lett. **88**, 262908 (2006).